Bulletin of Earthquake Engineering (2022) 20:6505–6526
https://doi.org/10.1007/s10518-022-01474-0

ORIGINAL ARTICLE

Investigation of seismic response of liquefiable canyon ground considering topography effect

Libo Xie[1] · Lei Su[1] · Hua-Ping Wan[2] · Xianzhang Ling[1]

Received: 14 July 2021 / Accepted: 5 July 2022 / Published online: 5 August 2022

Abstract
Topography effect is involved in the liquefiable canyon ground, which will cause variations of canyon slope displacement and liquefaction zone. To capture these salient response characteristics, a series of two-dimensional plane strain finite element models are created with various canyon sizes. Single soil stratum and constant water level are considered in these models, and detailed modeling techniques are presented. Computed static and dynamic results are illustrated and discussed. Effect of canyon size on initial horizontal stress disturbance region is explored. Specific attention should be paid to the remarkable changes in liquefaction location due to variation of canyon size, which can be used to estimate liquefaction zone. Modeling techniques and insights from this study are of significance to foundation design and liquefaction resistance.

Keywords Liquefiable canyon ground · Topography effect · Seismic response · Parametric analysis · Initial horizontal stress disturbance region

1 Introduction

Topography effect has been confirmed by a number of seismic records and post-earthquake investigations (Trifunac and Hudson 1971; Boore 1973; Spudich et al. 1996; Sepúlveda et al. 2005; Hough et al. 2010; Bard 2011). It has long been understood that the topography usually increases the amplitude of shaking at mountaintops and ridges, whereas canyons or valleys are capable of reducing ground motions (Gao et al. 2012).

✉ Lei Su
sulei@qut.edu.cn

Libo Xie
xielibo@qut.edu.cn

Hua-Ping Wan
hpwan@zju.edu.cn

Xianzhang Ling
lingxianzhang@qut.edu.cn

[1] School of Civil Engineering, Qingdao University of Technology, Qingdao, China

[2] College of Civil Engineering and Architecture, Zhejiang University, Hangzhou, China

Topography effect is of importance in the fields of seismology and earthquake engineering. To reveal the topography effect, a lot of research have carried out in these two fields. Mainly by methods of theoretical analysis and numerical simulation, seismologists reveal topography effect in various canyon shapes, such as semicylinder (Trifunac 1973), semiellipse (Wong and Trifunac 1974), trapezoid (Takemiya and Fujiwara 1994), V-shape (Tsaur et al. 2010), U-shape (Gao et al. 2012), and Gaussian shape (Ning et al. 2018). Scholars in the earthquake engineering mainly study the influence of canyon topography on engineering by numerical simulation. Solans et al. (2019) investigated the effect of canyon topography on ground motion for different soil profiles over a rigid bedrock using finite element (FE) method. Lu et al. (2020) explored influence of canyon on the propagation of railway vibration wave using FE method. Gao et al. (2020) presents the impact of ideal trapezium canyon topography on the stability of an earth-rockfill dam slope during earthquakes.

Research mentioned above have revealed importance of canyon topography effect. However, these researches did not consider the influence of sand liquefaction on topography effect. In fact, many infrastructures (e.g., bridge and dam) are often built on the liquefiable canyon ground with high water level. Post-earthquake investigations indicated that infrastructures built on liquefiable canyon ground are prone to damage (Hamada et al. 1987; Moss et al. 2011; Finn et al. 1996; Zhou et al. 2020; Cubrinovski et al., 2016; Hidayat et al. 2020). Sand liquefaction during earthquake is one of the main reasons for infrastructure failure (Finn et al. 1996; Finn and Fujit, 2002; Ashour and Ardalan 2011; Hidayat et al. 2020). As such, it is necessary to study the topography effect of liquefiable canyon ground, aiming to provide a reference for seismic design of infrastructures and measure of liquefaction mitigation.

To investigate the topography effect of liquefiable canyon ground, 13 FE models for liquefiable canyon site are created in this study. Specifically, a benchmark model is first developed. And then, 12 different models are created by changing canyon size based on the benchmark model. All 13 models are created via OpenSees, an object-oriented open-source software framework (http://opensees.berkeley.edu/, McKenna and Fenves 2001), which is widely employed to simulate dynamic response of ground and structure subjected to earthquake. In this study, influence of canyon size on initial horizontal stress disturbance region (IHSDR)is discussed, and canyon topography effect on slope displacement and acceleration, as well as the location of liquefaction zone is explored.

2 Benchmark finite element model

2.1 Computational domain

As shown in Fig. 1a, the benchmark finite element (FE) model is a 2D plane strain model with the computational domain of 260 m (length) × 50 m (height). The coordinate origin is located at the midpoint of model bottom, and the water level elevation is 40 m. The canyon in this model is idealized into an inverted trapezoid with a depth of 15 m, a bottom width of 30 m, and a top width of 100 m. To clearly demonstrate the computed results, the representative locations at the left boundary (blue solid circles) are marked in Fig. 1a.

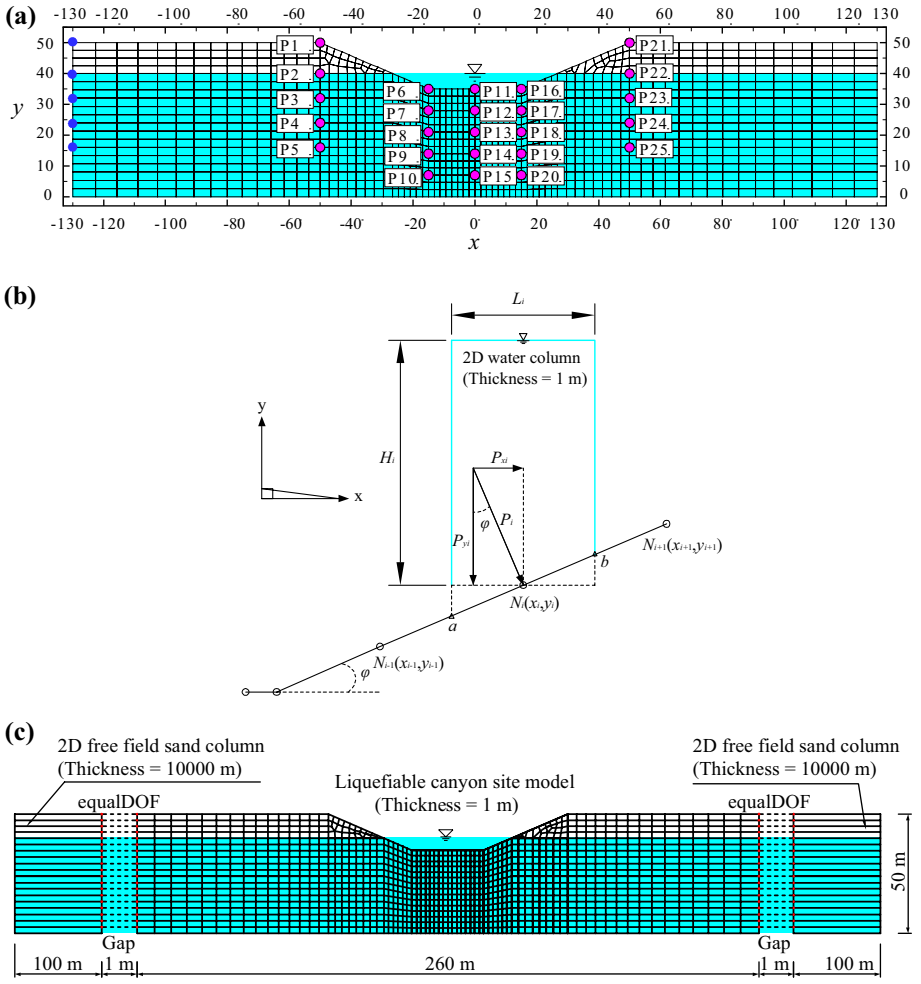

Fig. 1 2D finite element modeling of liquefiable canyon ground: **a** computational domain; **b** modeling of free water; **c** modeling of boundary conditions

2.2 Modeling of soil stratum

To avoid the interference of soil strata each other, the profile of liquefiable canyon site is simplified into a single soil stratum, comprising of medium sand only. Seismic response of such sand stratum is reproduced by pressure sensitive elastic-plastic constitutive model (i.e., PressureDependMultiYield material in OpenSees). Model parameters of medium sand are summarized in Table 1, referring to Yang et al. (2008). Default values were used for other parameters in this constitutive model. The quadUP element in OpenSees (i.e., Four-node plane-strain solid-fluid fully coupled element) is employed to simulate seismic response of medium sand, and the parameters associated to such element are summarized in Table 2.

Table 1 Model parameters of medium sand

Parameters	Value
Saturated soil mass density (t/m^3)	1.92
Reference shear modulus (kPa)	7.5×10^4
Reference bulk modulus (kPa)	2.0×10^5
Friction angle (degree)	33
Peak shear strain	0.1
Reference pressure (kPa)	80
Pressure dependence coefficient	0.5
Phase transformation angle (degree)	27
Contraction parameter	0.07
Initial void ratio	0.6

Table 2 Parameters of quadUP element

Parameters	Value
Element thickness (m)	1.0
Bulk modulus of fluid phase (kPa)	2.2×10^6
Fluid mass density (t/m^3)	1.0
Permeability coefficient in x-direction (m/s)	1.0×10^{-6} (1.0)
Permeability coefficient in y-direction (m/s)	1.0×10^{-6} (1.0)
Gravity acceleration component in y-direction (m/s^2)	− 9.81

Permeability coefficients in both x and y directions are different for static and dynamic analysis steps. Values outside parentheses represent the actual ones for dynamic analysis, while those inside parentheses are used for static analysis to quickly reach the initial state

2.3 Modeling of free water

Modeling of free water in the canyon is achieved by applying nodal force and hydrostatic pressure on the canyon boundary nodes in contact with free water. The purpose of applying nodal force and hydrostatic pressure is to reproduce effective stress and pore water pressure (PWP) in the sand stratum, respectively. Particularly, dynamic effect of free water during earthquake cannot been considered in this modeling technique. As such, applied nodal force and hydrostatic pressure remain constant in all analysis steps. The modeling technique for free water is further illustrated in the following.

The method of applying nodal force on the nodes of canyon boundary is depicted in Fig. 1b. According to the mesh of canyon boundary, a 2D rectangular water column with a height of H_i, a width of L_i and a thickness of 1 m, is applied at the node N_i (x_i, y_i). Herein, H_i is the height from canyon boundary node to free water surface, and H_w is the elevation of free water surface. Therefore, H_i can be obtained by

$$H_i = H_w - y_i \tag{1}$$

Furthermore, from Fig. 1b, L_i is the projection of line ab in the x direction. Point a is the midpoint of line $N_{i-1}N_i$, and point b is the midpoint of line $N_i\,N_{i+1}$. The coordinates of N_{i-1} and N_{i+1} are (x_{i-1}, y_{i-1}) and (x_{i+1}, y_{i+1}) respectively. L_i can be calculated by

$$L_i = \frac{\left(x_{i+1} - x_i\right) + \left(x_i - x_{i-1}\right)}{2} \tag{2}$$

The nodal force P_i acting on the canyon boundary node N_i can be calculated by Eq. (3). Its direction is perpendicular to the acting surface.

$$P_i = \rho_w g L_i H_i \tag{3}$$

where ρ_w is the density of free water (1.0 t/m^3), and g is the acceleration of gravity (9.81 m/s^2). The components of P_i in the x and y directions are P_{ix} and P_{iy}, respectively, can be determined by

$$P_{ix} = \rho_w g L_i H_i \sin\varphi \tag{4}$$

$$P_{iy} = \rho_w g L_i H_i \cos\varphi \tag{5}$$

where ϕ is the angle between inclined plane and x-axis. The applied hydrostatic pressure at the canyon boundary node N_i (x_i, y_i) can be computed by

$$u_{0i} = \rho_w g H_i \tag{6}$$

2.4 Staged analysis and input motion

To simulate dynamic behavior of sand stratum before and during earthquake, a staged analysis is utilized for the benchmark FE model of liquefiable canyon site. Overall, static analysis of model is carried out firstly to obtain appropriate initial states, and then dynamic analysis of model is performed to attain dynamic response of model during earthquake. Specifically, the simulation of liquefiable canyon site is accomplished through the following four steps. Among them, the first three steps are static analysis, and the final step is dynamic analysis. The details of these four steps are presented in the following.

Step 1: The permeability coefficients of sand stratum in both x and y directions are set to higher values (i.e., 1.0 m/s, see in Table 2) to rapidly achieve initial state. The self-weight is applied to the entire domain, and at the same time, nodal force and hydrostatic pressure are applied at the nodes, located at the slope and bottom of canyon, which in contact with free water. Then, elastic analysis is performed, and a stable non-zero stress field and a non-zero displacement field will be achieved.

Step 2: Based on the previous analysis, the initial state analysis is performed to maintain a stable non-zero stress field and obtain a zero-displacement field in the whole model.

Step 3: On the basis of the above analysis, the material property is updated to change the properties of sand stratum from elastic to plastic and plastic analysis is performed. As such, the stable stress and displacement fields obtained by plastic analysis are taken as initial conditions during dynamic analysis.

Step 4: The permeability of sand stratum is updated to actual values (i.e., 1.0×10^{-6} m/s, see in Table 2) firstly. Then, dynamic analysis is carried out by imparting one horizontal base excitation at the bottom of model. This base excitation comes from 1994 Northridge earthquake Rinaldi Receiving Station record (Component S48W) with scaled amplitude of 0.16 g, shown in Fig. 2. Such excitation has a relatively high pulse acceleration, which produces a significant level of nonlinear response and induces the obvious permanent deformation of canyon site.

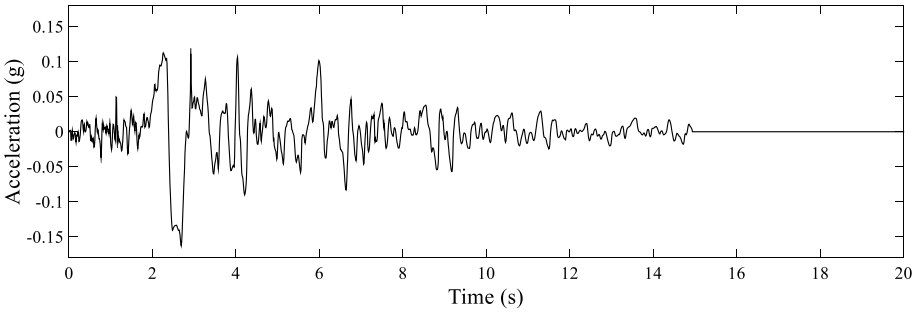

Fig. 2 Base excitation

2.5 Boundary conditions

In the FE numerical simulation of geotechnical earthquake engineering, free field boundary can well reproduce model boundary response, and be widely used in the numerical simulation (Su et al. 2020). To reproduce boundary response of canyon site, free field boundary is employed in this study. As shown in Fig. 1c, constraint conditions of canyon site model and modeling details of free field boundary are summarized as follows.

Firstly, a 2D free field sand column model with large mass is added, located 1 m from the left and right boundaries of canyon site model (Fig. 1c). In particular, the gap size (i.e., 1 m) between sand column and canyon site model boundaries is no practical meaning, which only kept independent each other during static analysis. The size of this sand column model is 100 m (width) × 50 m (height) × 10,000 m (thickness) to achieve a huge mass. Number of nodes at the boundary of sand column model is the same as that of canyon site model, and the elevations of adjacent nodes are equal. Sand column and canyon site models have the same material and element properties (Tables 1 and 2), and the same ground water level elevation. Therefore, degree of freedom (DOF) constraint of PWP is imposed on the nodes above water level for sand column and canyon site models.

Secondly, shear beam boundary condition is applied to sand column model. It includes: (i) constraint of displacement DOF in the x and y directions is imposed on the base nodes of sand column model; (ii) nodes with the same elevation on the boundary of sand column model (except bottom nodes) are constrained to the same displacement DOF in the x and y directions through equal DOF constraint.

Thirdly, sand column and canyon site models are kept independent during static analysis. The constraint of displacement DOF in the x and y directions is imposed on the base nodes of sand column and canyon site models.

Finally, sand column model is added at the left and right boundaries of canyon site model through equal DOF constraint before the dynamic analysis. In other words, the nodes at the same elevation on the adjacent boundaries of sand column and canyon site models (except bottom nodes) are constrained to the same translation in the x and y directions.

To verify the effectiveness of free field boundary, a base excitation (Fig. 2) is applied to 2D free field sand column model alone and canyon site model with 2D free field sand column model. Figure 3 shows relative horizontal displacement and absolute horizontal acceleration time histories of recoded locations (i.e., blue solid circle shown in Fig. 1). These time histories are derived from 2D free field sand column model alone and canyon site model with 2D free field sand column model. It can be observed from Fig. 3 that seismic

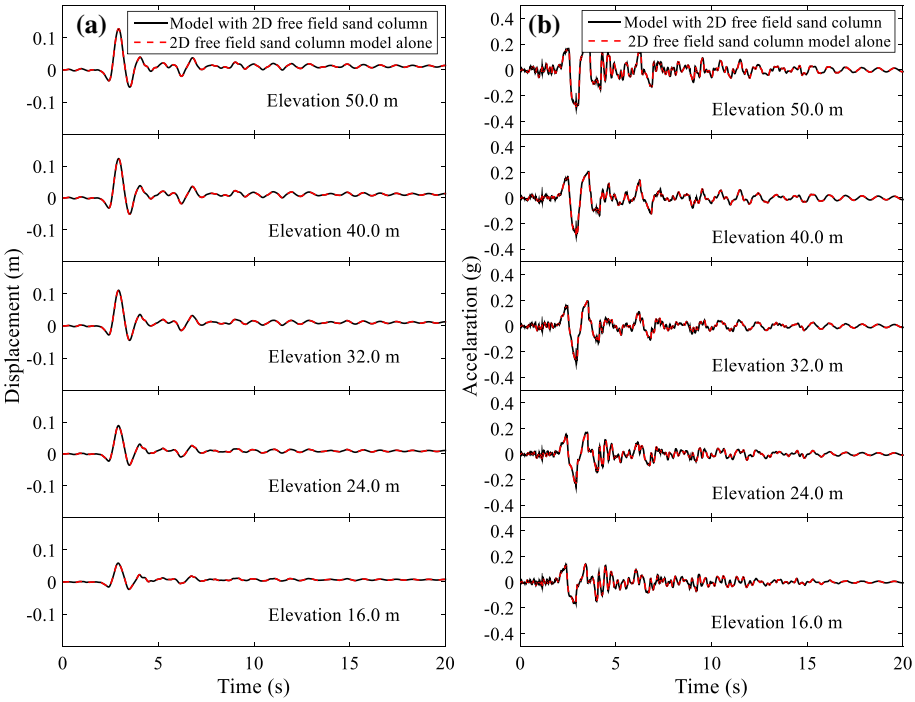

Fig. 3 Time histories of displacement and acceleration for each recorded point on the left boundary (shown in Fig. 1): **a** relative horizontal displacement; **b** absolute horizontal acceleration

response of 2D free field sand column model alone is the same as that of canyon site model with 2D free field sand column model. It is verified that the proposed free field boundary modeling technique is effective.

3 Computed results of benchmark model

3.1 Static analysis

The displacement contour obtained through static analysis is illustrated in Fig. 4a. From Fig. 4a, the following observations are made: (i) non-zero horizontal and vertical displacement contour for entire model are attained in the first analysis step; (ii) zero horizontal and vertical displacement contour are obtained in the second analysis step; (iii) horizontal and vertical displacements around the canyon in the third analysis step are all zero, except for small displacement (10^{-5} m) at the model boundary. The stress contour obtained in the third analysis step is presented in Fig. 4b. This shows: (1) vertical effective stress contour fluctuates with topography and obviously depends on depth; (2) AV of horizontal effective stress becomes greater near canyon; (3) shear stress contour forms a circular diffusion distribution at a certain depth due to canyon slope; (4) static PWP is zero above water level, while it presents a linear distribution as the depth increases below water level; (5) stress ratio (Yang et al. 2008) is higher at the bottom and boundary of canyon, in which sand stratum is closer to plastic

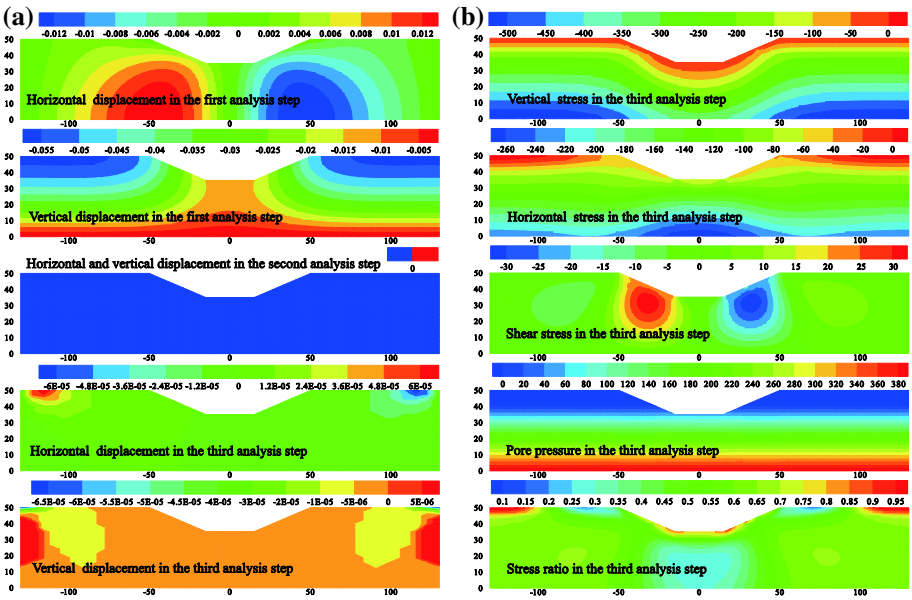

Fig. 4 Initial conditions of the benchmark model: **a** displacement contour in the first three analysis steps (unit: m); **b** stress contour in the third analysis step (unit: kPa)

state. Therefore, it can be concluded that displacement and stress contour obtained in the third analysis step conform to the initial state of canyon site model and can be used as initial condition for dynamic analysis.

Figure 4b reveals that the absolute values (AV) of horizontal stress is greater than that of vertical stress near the canyon. This indicates that there is an initial horizontal stress disturbance region (IHSDR) near the canyon due to the existence of canyon. The IHSDR will have an adverse effect on the stability of the canyon slope, so it is necessary to determine its range. The IHSDR is defined as the region where the AV(horizontal stress)-AV(vertical stress) > 0. The horizontal and vertical stress at the coordinates (0, 0), (0, 5), (0, 10), (0.15), (0,20), (0,25), (0,30), (0,35) are extracted, as shown in Fig. 5. Overall, AVs of horizontal and vertical stress decrease with increase of recorded point elevation. Horizontal stress is more sensitive to the change of elevation. The intersection point of two curves (i.e., AV(horizontal stress)-AV(vertical stress) = 0) is located at an elevation of 12.64 m. Furthermore, the IHSDR is marked in red in Fig. 6a. To further characterize the IHSDR, size parameter of canyon is defined by h, b, and B, and size parameter of IHSDR is defined by h_1, h_2, b_1, b_2, shown in Fig. 6b. Therefore, for benchmark model with h = 15 m, b = 30 m, B = 100 m, size parameters of IHSDR can be obtained as follows: h_1 = 22.36 m, h_2 = 16.66 m, b_1 = 20.56 m, b_2 = 13.83 m. It can be inferred that the existence of canyon is important factor for IHSDR. The correlation between size of canyon and size of IHSDR will be discussed in Sect. 4.1.

3.2 Dynamic analysis

Mesh deformation and displacement vector of benchmark model are illustrated in Fig. 7 at the maximum horizontal displacement of left boundary (i.e., t = 2.9 s) and the end

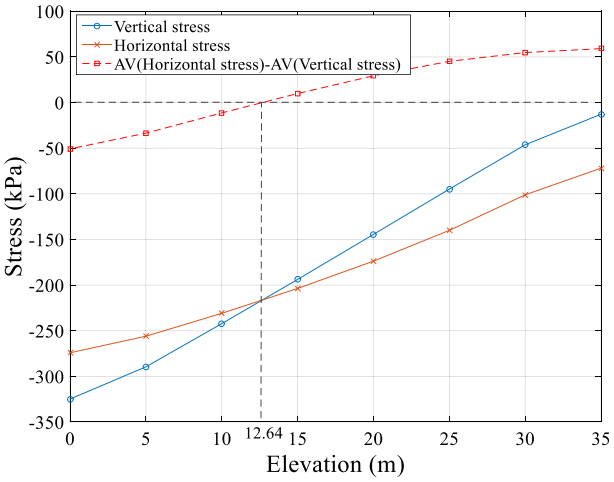

Fig. 5 Horizontal and vertical stresses with elevation (Note: AV represents absolute value)

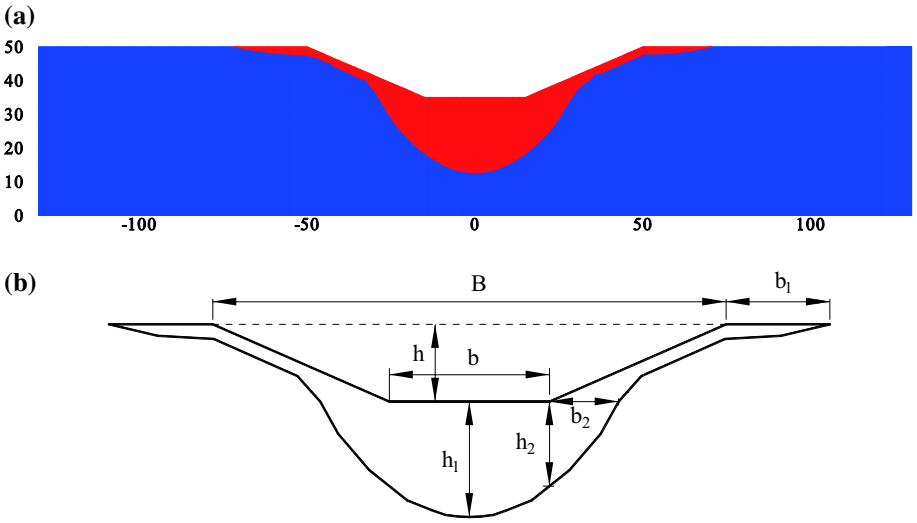

Fig. 6 IHSDR (red): **a** computed static results; **b** size parameters

of shaking (i.e., t = 20 s). At t = 2.9 s, the whole model tilts to right, which presents the characteristic of shear beam boundary. Canyon bottom and left side slope move upwards slightly, and ground surface except of canyon subsides slightly, as shown in Fig. 7a. At t = 20 s, canyon is squeezed and becomes narrower and shallower, and settlement of ground surface becomes larger, as shown in Fig. 7b.

Post-earthquake investigation shows that the liquefaction-induced lateral spreading is one of the main causes of structural instability and failure along rivers and offshore areas (Finn 2005; Bhattacharya and Madabhushi 2008). In these areas, extensive ground damage caused by the liquefaction-induced lateral spreading has resulted in the destruction of buildings, buried pipeline, ports, and wharves (Audemard et al. 2004; Holzer

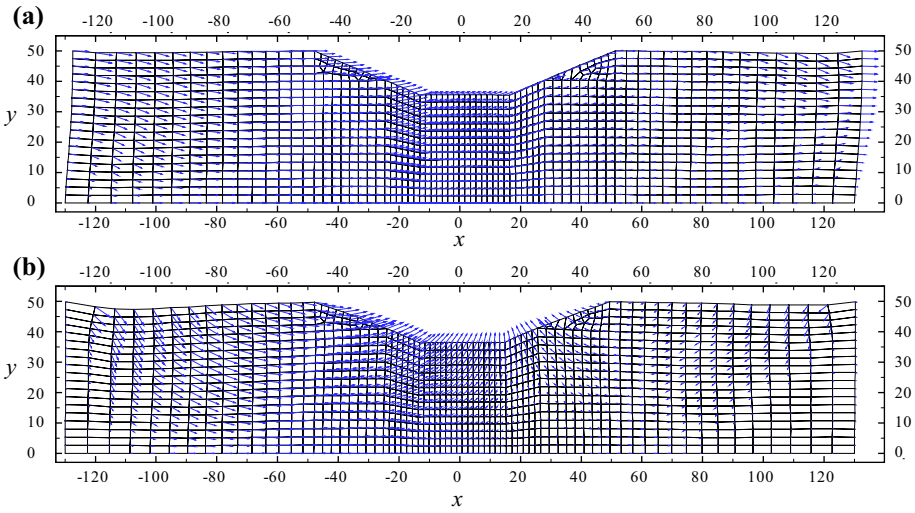

Fig. 7 Mesh deformation and displacement vector of the benchmark model (factor of 20): **a** t = 2.9 s; **b** t = 20 s

et al. 2004; Palermo et al. 2011; Haskell et al. 2013). The permanent ground displacement caused by the liquefaction-induced lateral spreading includes horizontal and vertical displacement. In particular, the permanent horizontal displacement is the root cause of canyon slope instability and infrastructure failure built on liquefiable canyon sites. Therefore, the horizontal displacement of the liquefiable canyon site during earthquake will be one of the focuses of the subsequent analysis.

For demonstration in convenience, 25 recorded points are marked in Fig. 1a, where P1–P5 and P21–P25 locate on the vertical lines which pass through left and right slope crests, respectively (elevation is 50 m, 40 m, 28 m, 24 m, 16 m in sequence). P11–P15, P6–P10, and P16–P20 locate on the vertical lines which pass through midpoint of canyon bottom, left and right slope toes, respectively (elevation is 35 m, 28 m, 21 m, 14 m, 7 m in sequence).

Figure 8a presents horizontal displacement time histories of 25 recorded points in Fig. 1a. In Fig. 8a, horizontal displacement time histories of all recorded points show the consistent trend. To clearly analyze displacement response, maximum and residual displacements of each recorded point are extracted in Fig. 8b and c. The slope of both maximum and residual displacements changes significantly at P2 and P22, which may be related to the existence of water level. Further discussion is presented in Sect. 4.2.1.

Figure 9 illustrates excess pore water pressure (EPWP) and excess pore water pressure ratio (EPWPR) time histories of all underwater recorded points in Fig. 1a. From Fig. 9, EPWPs show the obvious difference, and EPWPs significantly depend on the elevation. Compared with EPWPs, difference of EPWPRs is not noticeable (Fig. 9). From Fig. 9b, fluctuation of EPWPRs is sharper at the recorded points closer to canyon bottom, especially near the slope toe (e.g., P7, P17). This suggests that the presence of canyon has a great influence on the EPWPRs for canyon bottom region. Further, fluctuation of EPWPRs is related to the distance from recorded point to canyon bottom. As such, further discussion is presented in Sect. 4.2.2 to explore the effect of canyon size on EPWPR.

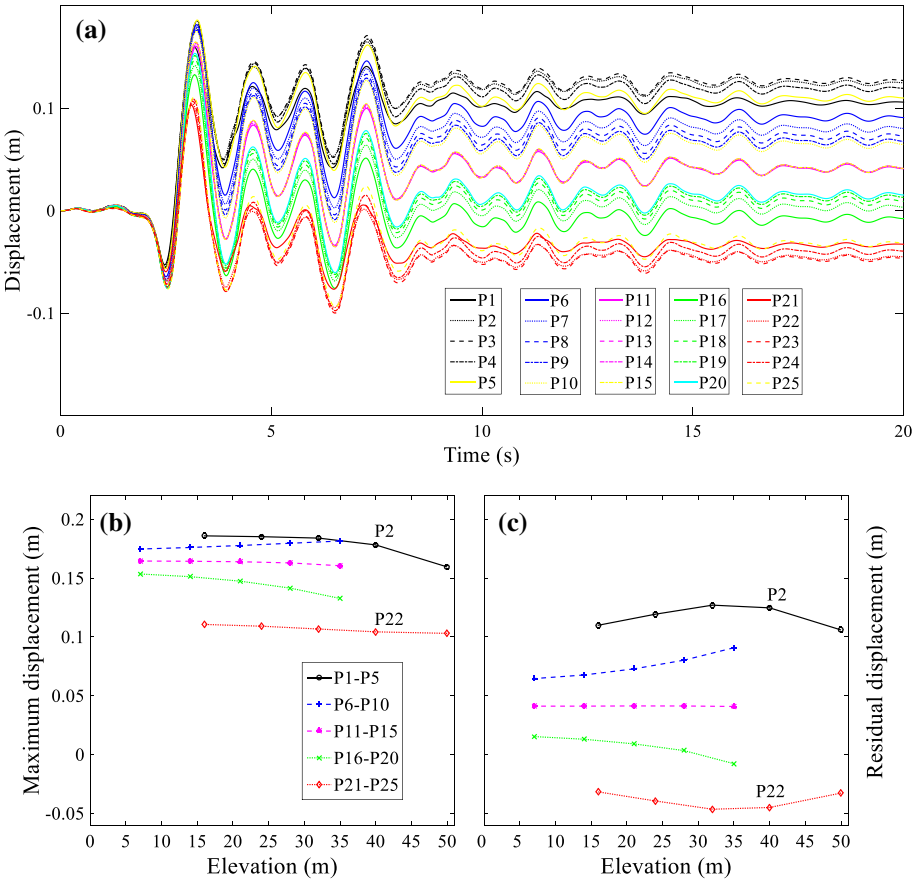

Fig. 8 Horizontal displacement: **a** time histories; **b** maximum values; **c** residual values

4 Parametric analysis

To study the influence of canyon size on IHSDR, horizontal displacement and EPWPR, additional 12 liquefiable canyon site models are created by changing canyon size parameters based on the benchmark model. All these models have the same overall size, material properties, boundaries and load conditions as the benchmark model. The canyon dimension parameter combinations of all 13 models are summarized in Table 3. To avoid the interaction effect of canyon size and sand model parameter, all canyon models (13 models in total) employ single medium sand stratum with the same model parameters.

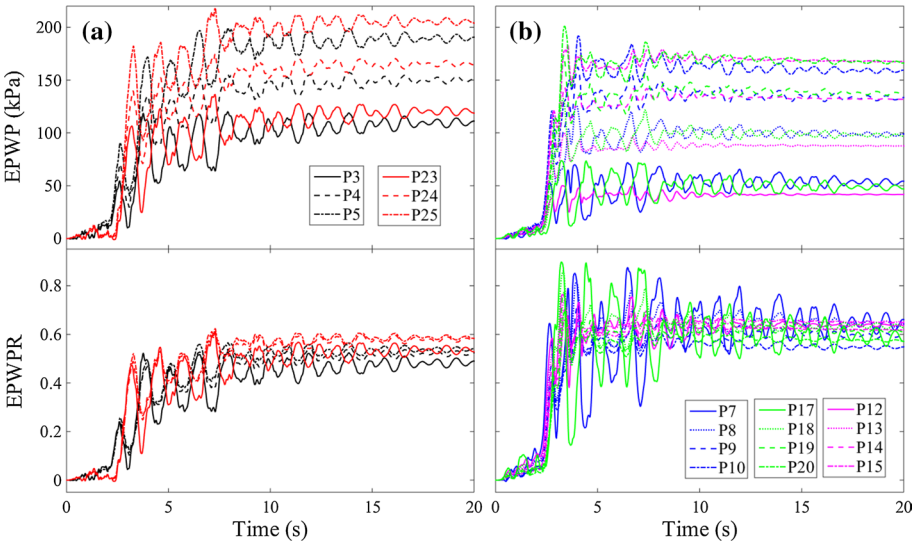

Fig. 9 EPWP and EPWPR time histories for various locations: **a** P3–P5 and P23–P25; **b** P7–P10, P12–P15, and P17–P20

Table 3 Combination of canyon size parameter

Case No.	h (m)	b (m)	B (m)	Slope angle (°)	Section area (m^2)	Description
1	15	30	100	23.2	975	Benchmark
2	0	0	0	0.0	0	Change h
3	5	30	100	8.1	325	
4	10	30	100	15.9	650	
5	20	30	100	29.7	1300	
6	15	10	100	18.4	825	Change b
7	15	20	100	20.6	900	
8	15	40	100	26.6	1050	
9	15	50	100	31.0	1125	
10	15	30	80	31.0	825	Change B
11	15	30	120	18.4	1125	
12	15	30	140	15.3	1275	
13	15	30	160	13.0	1425	

When the depth of the canyon is 0 m, 5 and 10 m, there is no free water in canyon

4.1 Static response

4.1.1 Influence of canyon depth (h) on size parameter of IHSDR

Figure 10 shows the horizontal and vertical stress contour for Cases 1–5 (Table 3) before shaking. When h = 0 m, the horizontal and vertical stress demonstrate a horizontal pattern. From Fig. 10a, the horizontal stress is closely related to canyon topography.

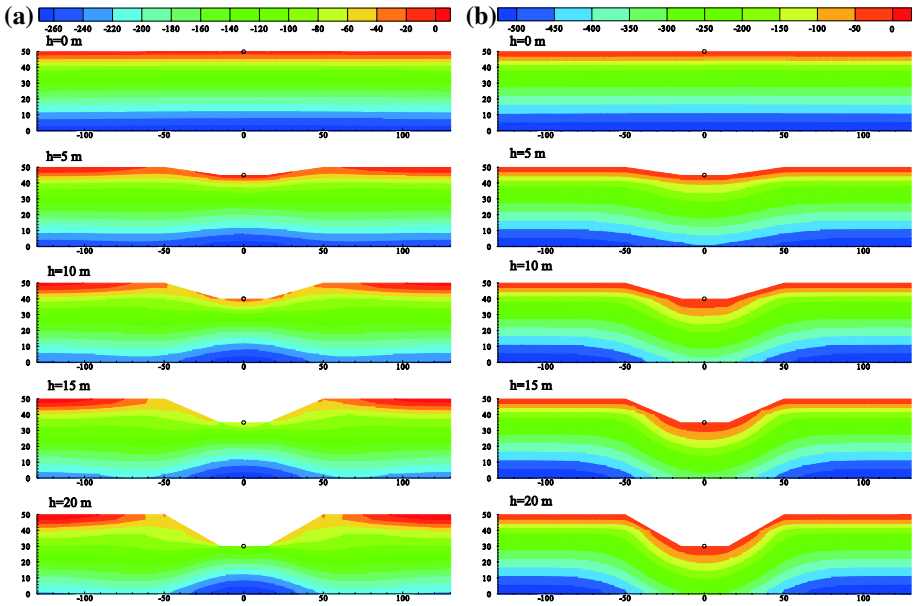

Fig. 10 Initial stress filed for Cases 1–5 (unit: kPa): **a** horizontal stress; **b** vertical stress

Specifically, with the increase of canyon depth (h), the horizontal stress increases near canyon. The vertical stress only depends on depth obviously from Fig. 10b. To further illustrate the difference of horizontal and vertical stress, the horizontal and vertical stress of canyon bottom midpoint, which is marked by a black circle (Fig. 10), are extracted. The relationship between these stresses and canyon depth (h) is plotted, shown in Fig. 11. From Fig. 11, the vertical stress remains relatively stable, but the horizontal stress increases rapidly with increase of canyon depth (h). A critical canyon depth (h_{cr}) is 5.513 m, at which is that the horizontal stress equals to the vertical stress.

Fig. 11 Horizontal and vertical stresses with canyon depth

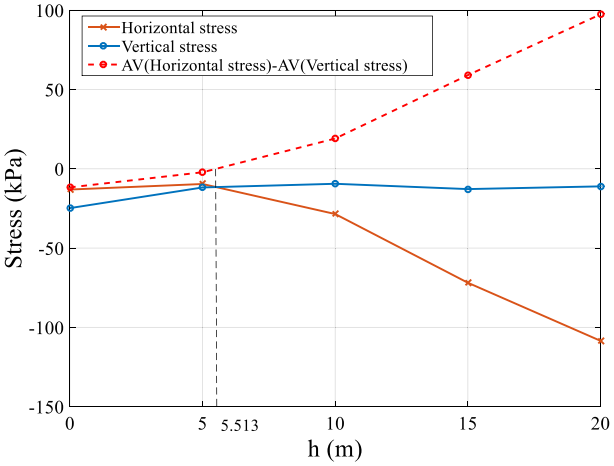

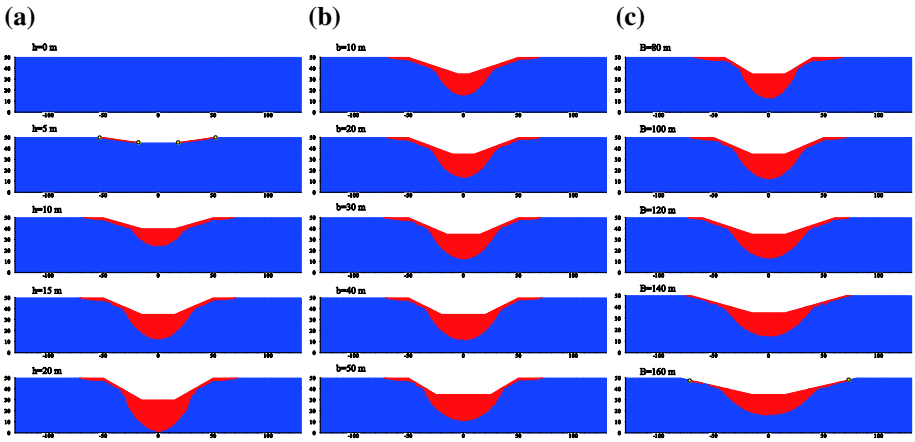

Fig. 12 IHSDR (red): **a** Cases 1–5; **b** Cases 1, 6–9; **c** Cases 1, 10–13

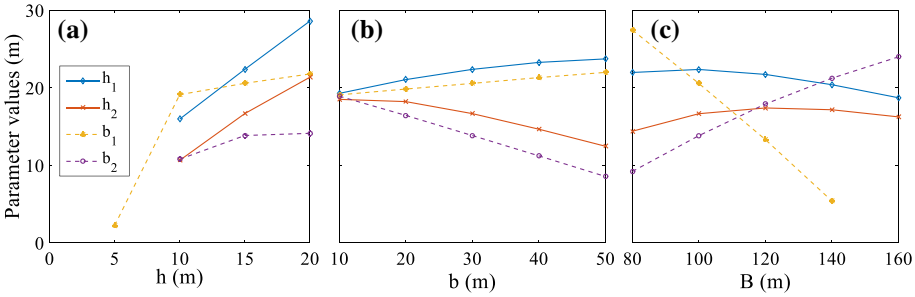

Fig. 13 Influence of canyon size on IHSDR: **a** canyon depth; **b** canyon bottom width; **c** canyon top width

When canyon depth (h) changes only, IHSDR for every case is shown in red in Fig. 12a. From Fig. 12a, IHSDR expands continuously with increase of canyon depth (h). When canyon depth h = 5 m, IHSDR extends to the yellow solid circles (Fig. 12a). According to parameter marked in Fig. 6b, the relation between canyon depth (h) and size parameter of IHSDR is drawn in Fig. 13a. When h∈[10, 20], the parameters h_1 and h_2 are sensitive to the change of h. When h∈[5, 10], the parameter b_1 is very sensitive to the change of h. In summary, canyon depth (h) has different effect on different IHSDR size parameters.

4.1.2 Influence of canyon bottom width (b) on size parameter of IHSDR

Figure 12b illustrates IHSDR under different canyon bottom widths (b) for Cases 1, 6–9 (Table 3). IHSDR continues to expand laterally at the canyon bottom with increase of canyon bottom. According to parameter marked in Fig. 6b, the relation between canyon bottom width (b) and size parameter of IHSDR is plotted in Fig. 13b. From Fig. 13b, the parameters h_1, h_2, b_1, and b_2 are obviously correlated with canyon bottom width (b), and the parameter b_2 is most sensitive to canyon bottom width (b). In short, IHSDR is noticeably influenced by canyon bottom width (b).

4.1.3 Influence of canyon top width (B) on size parameter of IHSDR

Figure 12c gives IHSDR under different canyon top widths (B) for Cases 1, 10–13 (Table 3). IHSDR expands laterally near canyon bottom and shrinks near slope crest with increase of canyon top width (B), shown in Fig. 13c. From Fig. 13c, IHSDR moves down along slope to position of marked yellow circles when canyon top width (B) is 160 m. According to parameter marked in Fig. 6b, the relation between canyon top width (B) and size parameter of IHSDR is illustrated in Fig. 13c. The parameter b_1 is the most sensitive to canyon top width (B), followed by parameter b_2, and parameters h_1 and h_2 are the least sensitive to canyon top width (B). In particular, there is a critical canyon top width B_{cr} (i.e., 152.63 m), when parameter b_1 is zero. In brief, IHSDR significantly depends on canyon top width (B).

The conclusions about influence of canyon size parameter on IHSDR size parameter are as follows: (i) the parameters h_1, b_2, and b_1 are the most sensitive to depth, bottom width, and top width of canyon, respectively; (ii) depth, bottom width, and top width of canyon mainly affects expansion of IHSDR along depth, slope toe, and slope crest, respectively.

4.2 Dynamic response

4.2.1 Influence of canyon size parameter on horizontal displacement and acceleration

Horizontal displacement time histories of P1-P5 and P21-P25 for Cases 1–5 (Table 3) are shown in Fig. 14, which indicates that horizontal displacement of each recorded point is affected by canyon depth (h). For demonstration convenience, maximum and

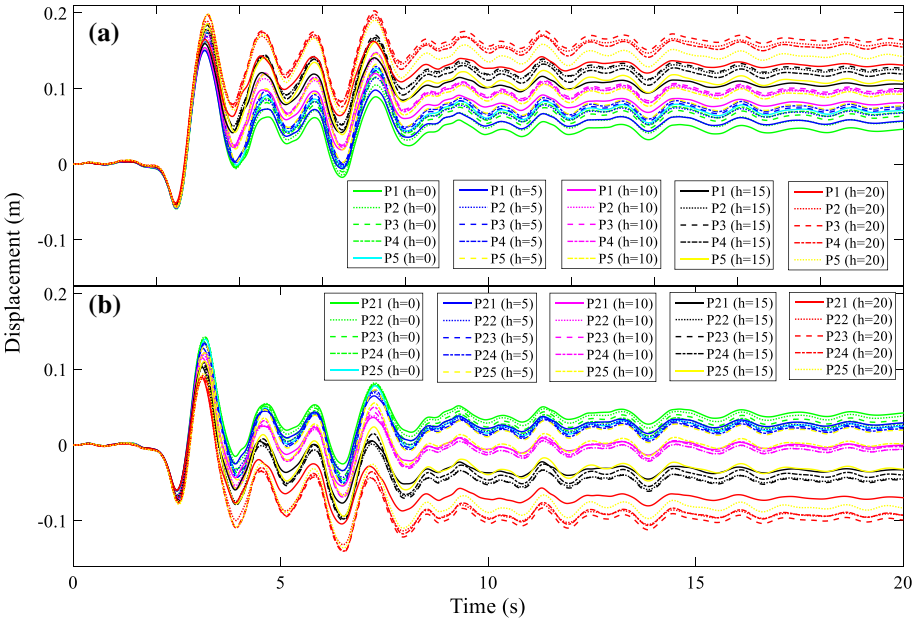

Fig. 14 Horizontal displacement time histories of recorded points for Cases 1–5 (Table 3): **a** P1–P5; **b** P21–P25

residual displacements of each recorded point with different canyon depths (h) are extracted in Fig. 15a and b. From Fig. 15a, when canyon depth (h) is zero, the slope of maximum displacement still presents an obvious change at P2 and P22. This change is mainly related to water level. Compared with saturated sand below water level, shear strength of sand above water level is higher, so shear deformation of recorded point above water level is smaller.

Using the same method, maximum and residual displacements of each recorded point are extracted in Fig. 15c–f for Cases 1, 6–13 (Table 3). By comparison, the influence of canyon depth (h) and top width (B) on horizontal displacement of recorded point is more obvious than that of canyon bottom width (b). The canyon depth (h) and top width (B) have the greatest influence on residual and maximum displacements, respectively. Canyon bottom width (b) has little influence on both maximum and residual displacements. From Fig. 15a–d, maximum and residual displacements increase with increase of canyon depth (h) or canyon bottom width (b) at P1-P5. On the contrary, maximum and residual displacements decrease with increase of canyon depth (h) or canyon bottom width (b) at P21–P25. Obviously, canyon slope becomes steeper with increase of canyon depth (h) or canyon bottom width (b). During shaking, maximum and residual displacements of left slope increase towards right direction, while maximum displacement of right slope decreases towards right direction and residual displacement increases towards left direction, which indicates that stability of slope becomes worse.

In Fig. 15e and f, maximum displacement decreases at P1–P5 and P21–P25 with increase of canyon bottom width (B), while residual displacement increases at P1–P5 and decreases at P21–P25. In fact, canyon slope decreases with increase of canyon bottom width (B). During shaking, maximum displacement of left and right slopes decreases towards right direction, which indicates that slope becomes more stable. However, residual displacement of left and right slopes towards canyon increases, which may be because the *x* coordinates of each recorded point change with increase of canyon top width (B).

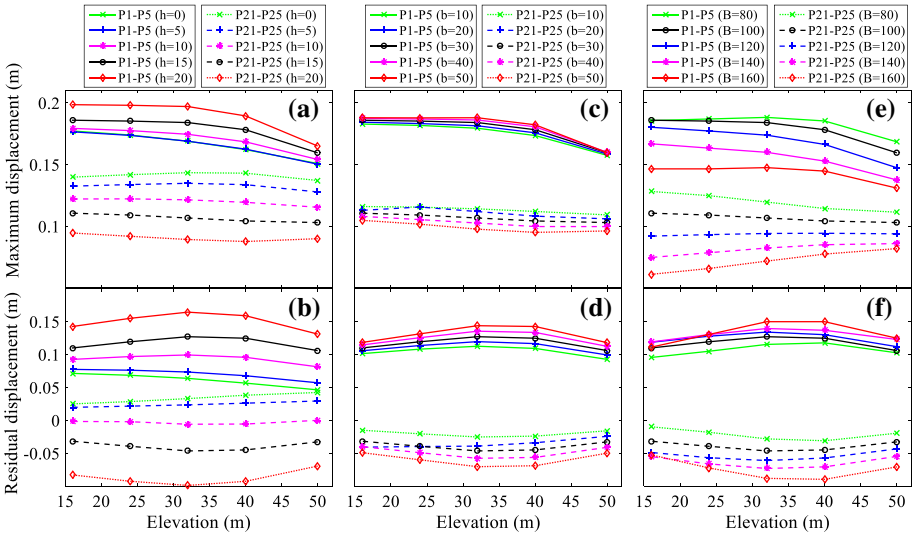

Fig. 15 Horizontal maximum and residual displacements of P1–P5 and P21–P25: **a** and **b** Cases 1–5; **c** and **d** Cases 1, and 6–9; **e** and **f** Cases 1, and 10–13

To quantify the impact of canyon size on seismic response of liquefiable ground, Fig. 16 illustrates the acceleration response spectrum and acceleration time history of all canyon models at the left slope crest P1 and left slope toe P6 as well as the corresponding acceleration amplification factor (AAF). From this figure, canyon topography effect cannot be clearly observed in the acceleration response spectrum (Fig. 16a, b, and c), but can be significantly observed in the acceleration time history (Fig. 16d, e, and f). Herein, the acceleration amplification effect is characterized by AAF. The AAFs of left slope toe (P6) and crest (P1), denoted by AAF(P6) and AAF(P1), are selected and discussed. In addition, AAF(P6)/AAF(P1) is used to characterize the amplification effect of acceleration at the slope toe relative to the slope crest, i.e., AAF(P6/P1).

From Fig. 16g, it can be found that the AAF(P6) is larger than AAF(P1) for Cases 1–5, which means that the seismic response at the slope toe is more severe than that at the slope crest. With the increase of h, AAF(P1) gradually decreases, AAF(P6) increases first and then decreases, and AAF(P6/P1) increases rapidly. It can be concluded that the acceleration response of the slope toe is larger comparing with the slope crest at the deeper canyon. It can also be found that AAF(P6/P1) is weakly affected by the canyon bottom width (Fig. 16 h), but is most strongly affected by the canyon top width, showing an increase first and then a sharp decrease with a peak at B = 100 m (Fig. 16i). However, when B = 160 m, the acceleration response at the slope crest is more significant than that at the slope toe. The

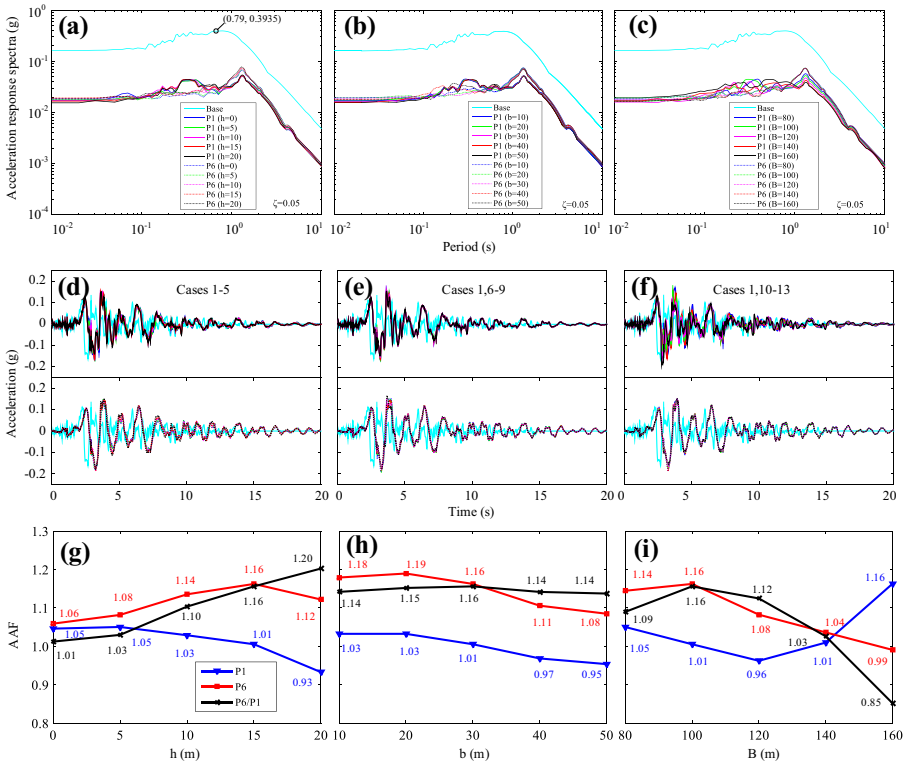

Fig. 16 Seismic response of canyon site for Cases 1–13 (Table 3) at P1 and P6: **a**, **b** and **c** acceleration response spectrum; **d**, **e** and **f** acceleration time history; **g**, **h** and **i** acceleration amplification factor

value of AAF(P6/P1) is greater than 1.0 in most cases. Therefore, in the seismic design, special attention should be paid to the amplification of the seismic action at the slope toe.

From Fig. 16g, h, and i, the value of AAF(P6) is between 0.99 and 1.19, and the value of AAF(P1) is between 0.93 and 1.16. The value of AAF(P6/P1) changes from 0.85 to 1.20. This indicates that there may be an amplification or de-amplification effect for base excitation in the different locations of canyon site. The maximum AAF(P1) is 1.16, and the maximum AAF(P6/P1) is 1.20, which conforms to the EC8 (i.e., Amplification Factors in EN-1998-5, Appendix A.2a).

The AAF(P6), AAF(P1), and AAF(P6/P1) against slope angle and canyon section area are shown in Fig. 17. From Fig. 17a, when the slope is greater than 15°, the PGA at the slope toe is significantly amplified. When the slope is less than 15°, the PGA at the slope crest is obviously amplified. From Fig. 17b, the AAF at the slope toe and crest changes with increase of canyon section area. In addition, it can also be found that acceleration amplification effect is also different for canyons with different sizes and the same slope angle (Cases 6 and 11 / Cases 9 and 10), or with different sizes and the same section area (Cases 6 and 10 / Cases 9 and 11). This shows that AAF of the slope toe and crest is significantly affected by the canyon topography. As such, the deeper and narrower canyon displays the stronger amplification effect at the slope toe, and the shallower and wider canyon illustrates the stronger amplification effect at the slope crest.

4.2.2 Influence of canyon size parameter on EPWPR

To investigate variation of EPWPR near canyon bottom with canyon size parameter, three recorded points (located below water level) are selected along different elevations on the midpoint of canyon bottom (MP), left slope toe point (LP), and right slope toe point (RP). The elevations of recorded points for every case are summarized in Table 4.For Cases 1–13 (Table 3), locations with EPWPR ≥ 1 for recorded points are listed in Table 4. It can be found that: (i) instantaneous liquefaction does not occur at the recorded point far from canyon bottom or the water level (i.e., blue solid circles); and (ii) instantaneous liquefaction is more likely to occur near slope toe compared with midpoint region of canyon bottom. Specifically, from Table 4, when only increasing canyon depth (h), instantaneous liquefaction first appears and then disappears nearest slope toe (i.e., black solid circles), while instantaneous liquefaction gradually appears slightly away from slope toe (i.e., red solid circles). This indicates that instantaneous liquefaction zone moves deeper from slope toe with increase of canyon depth (h). In Table 4, when only increasing canyon bottom width

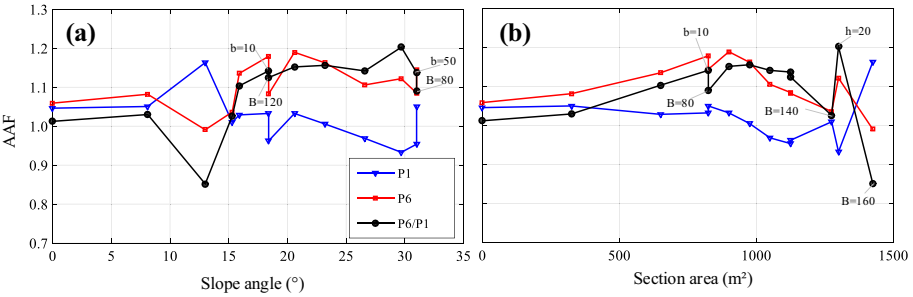

Fig. 17 AAF with canyon topography: **a** slope angle; **b** section area

Table 4 Locations with EPWPR ≥ 1 for variation of canyon depth (h)

h (m)	MP	LP	RP	MP	LP	RP	MP	LP	RP
	Elevation=37.3 m			Elevation=34.7 m			Elevation=32.0 m		
0	×	×	×	×	×	×	×	×	×
5	×	×	○	×	×	×	×	×	×
10	○	○	○	×	×	×	×	×	×
15	Elevation=32.7 m			Elevation=30.3 m			Elevation=28.0 m		
	×	×	×	×	○	○	×	×	×
20	Elevation=28.0 m			Elevation=26.0 m			Elevation=24.0 m		
	×	×	×	×	○	○	×	×	×
b (m)	MP	LP	RP	MP	LP	RP	MP	LP	RP
	Elevation=32.7 m			Elevation=30.3 m			Elevation=28.0 m		
10	×	×	×	×	×	×	×	×	×
20	×	×	×	×	○	×	×	×	×
30	×	×	×	×	○	○	×	×	×
40	×	×	×	×	○	○	×	×	×
50	×	×	×	×	○	○	×	×	×
B (m)	MP	LP	RP	MP	LP	RP	MP	LP	RP
	Elevation=32.7 m			Elevation=30.3 m			Elevation=28.0 m		
80	×	×	×	×	○	○	×	×	×
100	×	×	×	×	○	○	×	×	×
120	×	○	○	×	○	○	×	×	×
140	×	○	○	×	○	○	×	×	×
160	×	○	○	×	×	×	×	×	×

Note:

○ is EPWPR ≥ 1, instantaneous liquefaction.
× is EPWPR < 1, no liquefaction.

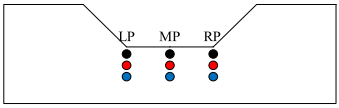

(b), there is no instantaneous liquefaction at the elevations of 32.7 m and 28.0 m. Instantaneous liquefaction only appears at the elevation of 30.3 m near the slope toe. This indicates that shear contraction effect is significantly enhanced only at the elevation of 30.3 m near slope toe with increase of canyon bottom width. From Table 4, when only increasing canyon top width (B), instantaneous liquefaction gradually appears at the elevation of 32.7 m near slope toe, while instantaneous liquefaction first appears and then disappears at the elevation of 30.3 m near slope toe. This indicates that instantaneous liquefaction zone expands and moves upward closer to slope toe with increase of canyon top width (B).

5 Discussions

Based on the above investigation, IHSDR appears around the canyon due to the existence of canyon. The correlation between IHSDR and topography parameter of canyon can provide a reference for design of slope support engineering. Similarly, the existence of canyon and variation of its topography size have significant impact on seismic response of liquefiable ground. Observations obtained in this study that instantaneous liquefaction zone moves with change of canyon topography size can provide a valuable guidance for seismic design

of pile foundation and design of liquefaction resistance in the liquefiable ground. Up to now, no direct evidence has been found for the influence of IHSDR on seismic response of liquefiable ground.

6 Summary and conclusions

Based on static computed results, the existence of canyon topography has significant impact on the distribution of initial stress field, especially horizontal stress field, which leads to formation of IHSDR around canyon. Specifically, canyon topography has a great influence on the IHSDR. Several main findings are summarized:

- The increase of canyon depth leads that horizontal stress exceeds vertical stress at a certain range around canyon. As such, canyon depth is a direct reason for IHSDR at the entire domain. Furthermore, the increase of canyon depth plays a major role in the expansion of IHSDR. A critical canyon depth (h_{cr}) for IHSDR is around 5.5 m. The influence of IHSDR on slope stability needs to be considered when the slope depth exceeds 5.5 m.
- The increase of canyon bottom width mainly leads to reduction of horizontal stress near slope toe, which plays an important role in the contraction of IHSDR.
- The increase of canyon top width mainly causes to reduction of horizontal stress near the toe and crest of slope, which plays a significant role in the contraction of IHSDR.

In light of dynamic computed results, canyon topography also has significant impact on seismic response of liquefiable ground, especially horizontal displacement and acceleration near slope and EPWPR near canyon bottom. The size of canyon topography has a great effect on maximum and residual displacements of slope, acceleration and formulation of instantaneous liquefaction zone. Several observations can be made:

- The influence of depth, bottom width, and top width of canyon on the residual displacement is consistent. The increase of all canyon size parameters can increase the residual displacement to varying degrees. The canyon depth has the greatest influence on the residual displacement, followed by canyon top width, and then canyon bottom width.
- The influence of depth, bottom width, and top width of canyon on the maximum displacement and acceleration is not consistent. The canyon top width has the greatest influence on maximum displacement and acceleration, followed by canyon depth, and then canyon bottom width.
- The acceleration amplification factor of the slope toe and crest is significantly affected by the canyon topography. The deeper and narrower canyon displays the stronger amplification effect at the slope toe, and the shallower and wider canyon illustrates the stronger amplification effect at the slope crest. An acceleration amplification factor is not less than 1.2, when the stability of canyon slope is verified during earthquake.
- Compared with the area near the midpoint of canyon bottom, shear contraction effect near slope toe is more obvious and instantaneous liquefaction is more likely to occur. With increase of canyon depth or bottom width, instantaneous liquefaction zone moves deeper from slope toe. With increase of canyon top width, instantaneous liquefaction zone moves upwards to slope toe. The instantaneous liquefaction occurs at deeper zone with the increase of slope angle.

Particularly, there are still some deficiencies in this study, such as, only one specific ground motion was considered, and influence of soil property parameters on topography effect has still not been explored. Therefore, the topographic effect of canyon site under different types of ground motion and the correlation between topography effect and constitutive model parameters of soil stratum will be investigated in the future study.

Acknowledgements The presented study is funded by the National Natural Science Foundation of China (42072310 and 51808307). These supports are gratefully acknowledged.

Authors contributions Libo Xie: Original draft preparation. Lei Su: Numerical modeling technique. Hua-Ping Wan: Data curation. Xianzhang Ling: Reviewing and editing.

Funding The presented study is funded by the National Natural Science Foundation of China (42072310 and 51808307).Conflict of interest The authors declare that they have no known competing financial interests or personal relationships that could have appeared to influence the work reported in this paper.

References

Ashour M, Ardalan H (2011) Piles in fully liquefied soils with lateral spread. Comput Geotech 38(6):821–833. https://doi.org/10.1016/j.compgeo.2011.05.001

Audemard MFA, Gómez JC, Tavera HJ, Orihuela GN (2004) Soil liquefaction during the Arequipa Mw 8.4, June 23, 2001 earthquake, southern coastal Peru. Eng Geol 78(3):237–255. https://doi.org/10.1016/j.enggeo.2004.12.007

Bard PY (2011) Seismic loading - engineering characterization of seismic ground motion and key controlling factors. Eur J Environ Civ Eng 15(Sup 1):141–184. https://doi.org/10.1080/19648189.2011.9695307

Bhattacharya S, Madabhushi SPG (2008) A critical review of methods for pile design in seismically liquefiable soils. Bull Earthq Eng 6(3):407–446. https://doi.org/10.1007/s10518-008-9068-3

Boore DM (1973) The effect of simple topography on seismic waves: implications for the accelerations recorded at Pacoima Dam, San Fernando Valley, California. Bull Seismol Soc Am 63(5):1603–1609. https://doi.org/10.1785/BSSA0630051603

Cubrinovski M, Robinson K (2016) Lateral spreading: evidence and interpretation from the 2010–2011 Christchurch earthquakes. Soil Dyn Earthq Eng 91:187–201. https://doi.org/10.1016/j.soildyn.2016.09.045

Finn WDL (2005) A study of piles during earthquakes: issues of design and analysis. Bull Earthq Eng 3(2):141–234. https://doi.org/10.1007/s10518-005-1241-3

Finn WDL, Fujita N (2002) Piles in liquefiable soils: seismic analysis and design issues. Soil Dyn Earthq Eng 22(9–12):731–742. https://doi.org/10.1016/S0267-7261(02)00094-5

Finn WDL, Byrne PM, Evans S, Law T (1996) Some geotechnical aspects of the Hyogo-ken Nanbu (Kobe) earthquake of January 17, 1995. Can J Civ Eng 23:778–796. https://doi.org/10.1139/l96-888

Gao YF, Zhang N, Li DY, Liu HL, Cai YQ, Wu YX (2012) Effects of topographic amplification induced by a U-shaped canyon on seismic waves. Bull Seismol Soc Am 102(4):1748–1763. https://doi.org/10.1785/0120110306

Gao YQ, Wang LY, Li DY, Gao YF (2020) Evaluation of valley topography effects on the seismic stability of earth-rockfill dams via a modified valley topography coefficient. Comput Geotech 128:103814. https://doi.org/10.1016/j.compgeo.2020.103814

Hamada M, Towhata I, Yasuda S, Isoyama R (1987) Study on permanent ground displacement induced by seismic liquefaction. Comput Geotech 4(4):197–220. https://doi.org/10.1016/0266-352X(87)90001-2

Haskell JJM, Madabhushi SPG, Cubrinovski M, Winkley A (2013) Lateral spreading-induced abutment rotation in the 2011 Christchurch earthquake: observations and analysis. Geotechnique 63(15):1310–1327. https://doi.org/10.1680/geot.12.P.174

Hidayat RF, Kiyota T, Tada N, Hayakawa J, Nawir H (2020) Reconnaissance on liquefaction-induced flow failure caused by the 2018 M_w 7.5 Sulawesi earthquake, Palu, Indonesia. J Eng Technological Sci 52(1):51–65. https://doi.org/10.5614/j.eng.technol.sci.2020.52.1.4

Holzer TL, Noce TE, Bennett MJ (2004) Liquefaction-induced lateral spreading in Oceano, California, during the 2003 San Simeon Earthquake. US Geological Survey

Hough SE, Altidor JR, Anglade D, Given D, Janvier MG, Maharrey JZ, Yong A (2010) Localized damage caused by topographic amplification during the 2010 M 7.0 Haiti earthquake. Nat Geosci 3(11):778–782. https://doi.org/10.1038/ngeo988

Lu H, Xiong L, Gao Z, Liang P, Wu B (2020) Effects of the canyon topography on railway environment vibrations. Proc Inst Civil Eng Forens Eng 172(3):87–96. https://doi.org/10.1680/jfoen.19.00019

McKenna FT, Fenves GL (2001) The OpenSees command language manual (Version 1.2). Pacific Earthquake Engineering Research Center, University of California, Berkeley, California

Moss RES, Kayen RE, Tong LY, Liu SY, Cai GJ, Wu J (2011) Retesting of liquefaction and nonliquefaction case histories from the 1976 Tangshan earthquake. J Geotech GeoEnviron Eng 137(4):334–343. https://doi.org/10.1061/(asce)gt.1943-5606.0000406

Ning L, Dai T, Wang L, Yuan S, Pang J (2018) Numerical investigation of Rayleigh-wave propagation on canyon topography using finite-difference method. J Appl Geophys 159:350–361. https://doi.org/10.1016/j.jappgeo.2018.09.007

Palermo A, Wotherspoon L, Wood J, Chapman H, Scott A, Hogan L, Kivell A, Camnasio E, Yashinsky M, Bruneau M, Chouw N (2011) Lessons learnt from 2011 Christchurch earthquakes: analysis and assessment of bridges. Bull New Z Soc Earthq Eng 44(4):319–333. https://doi.org/10.5459/bnzsee.44.4.319-333

Sepúlveda SA, Murphy W, Jibson RW, Petley DN (2005) Seismically induced rock slope failures resulting from topographic amplification of strong ground motions: the case of Pacoima Canyon, California. Eng Geol 80(3–4):336–348. https://doi.org/10.1016/j.enggeo.2005.07.004

Solans D, Skiada E, Kontoe S, Potts DM (2019) Canyon topography effects on ground motion: assessment of different soil stiffness profiles. Obras y Proyectos 25:51–58. https://doi.org/10.4067/s0718-28132019000100051

Spudich P, Hellweg M, Lee WHK (1996) Directional topographic site response at Tarzana observed in aftershocks of the 1994 Northridge, California, earthquake: implications for mainshock motions. Bull Seismol Soc Am 86(1B):S193–S208. https://doi.org/10.1785/BSSA08601BS193

Su L, Wan HP, Luo Y, Dong Y, Niu F, Lu J, Arulmoli AK (2020) Seismic performance assessment of a pile-supported wharf retrofitted with different slope strengthening strategies. Soil Dyn Earthq Eng 129:105903. https://doi.org/10.1016/j.soildyn.2019.105903

Takemiya H, Fujiwara A (1994) SH-wave scattering and propagation analyses at irregular sites by time domain BEM. Bull - Seismological Soc Am 84(5):1443–1455. https://doi.org/10.1016/0148-9062(95)93178-R

Trifunac MD (1973) Scattering of plane SH waves by a semi-cylindrical canyon. Earthq Eng Struct Dynamics 1(3):267–281. https://doi.org/10.1002/eqe.4290010307

Trifunac MD, Hudson DE (1971) Analysis of the Pacoima dam accelerogram-San Fernando, California, earthquake of 1971. Bull Seismol Soc Am 61(5):1393–1411. https://doi.org/10.1785/BSSA0610051393

Tsaur DH, Chang KH, Hsu MS (2010) An analytical approach for the scattering of SH waves by a symmetrical V-shaped canyon: Deep case. Geophys J Int 183(3):1501–1511. https://doi.org/10.1111/j.1365-246X.2010.04806.x

Wong HL, Trifunac MD (1974) Scattering of plane shear waves by a semi-elliptical canyon. Earthq Eng Struct Dynamics 3(2):157–169. https://doi.org/10.1002/eqe.4290030205

Yang Z, Lu J, Elgamal A (2008) OpenSees soil models and solid-fluid fully coupled elements.User's Manual Ver, 1.0.

Zhou YG, Xia P, Ling DS, Chen YM (2020) A liquefaction case study of gently sloping gravelly soil deposits in the near-fault region of the 2008 M_w 7.9 Wenchuan earthquake. Bull Earthq Eng 18(14):6181–6201. https://doi.org/10.1007/s10518-020-00939-4